Engineering antiferromagnetic skyrmions and antiskyrmions at metallic interfaces

Arnob Mukherjee [1], Deepak S. Kathyat [2], and Sanjeev Kumar [1]

[1]*Department of Physical Sciences, Indian Institute of Science Education and Research (IISER) Mohali,*
Sector 81, S.A.S. Nagar, Manauli PO 140306, India
[2]*Harish-Chandra Research Institute, HBNI, Chhatnag Road, Jhunsi, Allahabad 211019, India*

We identify a mechanism to convert skyrmions and antiskyrmions into their antiferromagnetic (AFM) counterparts via interface engineering. The key idea is to combine properties of an antiferromagnet and a spin-orbit (SO) coupled metal. Utilizing hybrid Monte Carlo (HMC) simulations for a generic microscopic electronic Hamiltonian for the interfacial layers, we explicitly show the emergence of AFM skyrmions and AFM antiskyrmions. We further show that an effective spin Hamiltonian provides a simpler understanding of the results. We discuss the role of electronic itinerancy in determining the nature of magnetic textures, and demonstrate that the mechanism also allows for a tuning of antiskyrmion size without changing the SO coupling.

I. INTRODUCTION

Magnetic skyrmions and antiskyrmions are topologically protected magnetization textures that have been observed in a number of chiral magnets. Their potential use as building blocks of next-generation spintronics devices has motivated numerous scientific studies [1–7]. Despite many advantages associated with skyrmions, such as, enhanced stability due to its topological protection [8–13], ultralow current density dynamics [14–18], and large Hall current [19,20], their transverse deflection upon application of current—known as skyrmion Hall effect—presents a major bottleneck for applications [21]. Therefore, reducing the transverse component of skyrmion velocity while retaining all of its favorable properties is an important goal of research in this field [22–24]. One of the approaches has been to tune the nature of the skyrmion state in such a way that the Magnus force gets intrinsically canceled [25–27]. These efforts have given rise to the concept of antiferromagnetic skyrmions [28–36].

While there are now a few examples of skyrmions in insulating magnets, these textures are mostly observed in metals [37–42]. Indeed, the property that skyrmions can be driven by ultralow currents comes into play only if the host material is a metal. Therefore the challenge is not only to convert skyrmions into antiferromagnetic skyrmions, but also to do so while retaining the metallic character of the host. Recent experiments report observation of antiferromagnetic skyrmions in metal—antiferromagnet interfaces, which can be driven efficiently by applying spin-orbit torque [43].

In this paper, we explicitly show that antiferromagnetic counterparts of skyrmions and antiskyrmions can be stabilized at the interface between an antiferromagnetic insulator and a spin-orbit coupled metal. While we only discuss the case of Dresselhaus metal here, the interface engineering approach to convert skyrmions into antiferromagnetic skyrmions is applicable in general for Bloch and Néel skyrmions as well as antiskyrmions. We also discuss the role of electronic hopping in determining the nature of the topological magnetic textures. The results are obtained via two qualitatively different methods: (i) hybrid Monte Carlo simulations that explicitly retain the itinerancy of electrons, and (ii) classical simulations of an effective spin Hamiltonian. These methods provide complementary insights into the underlying physics. While the first approach provides a direct accurate treatment of electronic model, the second offers a simpler understanding of the results.

II. MODEL

A schematic view of the model set-up is presented in Fig. 1 where the upper layer represents the bottom surface of an antiferromagnetic insulator and the lower one the top surface of a spin-orbit coupled metal. Note that the separation in the vertical direction is exaggerated for clarity. A prototype electronic Hamiltonian for such bilayers, with a specific choice of the type of SO coupling, is given by

$$H = -\sum_{\langle ij \rangle, \sigma} t_\gamma (c_{i\sigma}^\dagger c_{j\sigma} + \text{H.c.}) + \lambda \sum_i [i(c_{i\downarrow}^\dagger c_{i+x\uparrow} + c_{i\uparrow}^\dagger c_{i+x\downarrow})$$
$$+ (c_{i\downarrow}^\dagger c_{i+y\uparrow} - c_{i\uparrow}^\dagger c_{i+y\downarrow}) + \text{H.c.}] - J_H \sum_i \mathbf{S}_i \cdot \mathbf{s}_i$$
$$+ J_{AF} \sum_{\langle ij \rangle} \mathbf{S}_i \cdot \mathbf{S}_j, \tag{1}$$

where, $c_{i\sigma} (c_{i\sigma}^\dagger)$ annihilates (creates) an electron at site i with spin σ in the metallic layer. The first term represents electronic kinetic energy in terms of nearest-neighbor (nn) hopping t_γ from site i to site $j = i + \gamma$ with $\gamma = x, y$, and $|t_\gamma| = 1$ sets the basic energy scale, unless stated otherwise. The second term is Dresselhaus SO coupling of strength λ. $\mathbf{s}_i = (1/2) \sum_{\sigma, \sigma'} c_{i\sigma}^\dagger \boldsymbol{\sigma}_{\sigma\sigma'} c_{i\sigma'}$ is the electronic spin operator at site i, where, $\boldsymbol{\sigma} = (\sigma^x, \sigma^y, \sigma^z)$ is the vector of Pauli matrices.
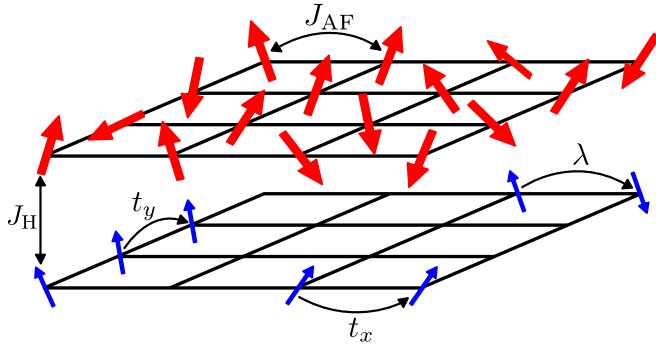
FIG. 1. Schematic view of the interface between a SO-coupled metal and an antiferromagnet. The upper layer consists of large magnetic moments (red arrows). The lower layer represents a SO-coupled 2DEG. J_{AF} denotes the AFM coupling between localized moments, $t_{x(y)}$ denote the spin-preserving hopping along $x(y)$ directions, and λ is the strength of SO coupling visualized as spin-flip hopping. J_H denotes the Hund's rule coupling between the local moments and the spins of itinerant electrons.

The last two terms represent the interlayer ferromagnetic and intralayer antiferromagnetic couplings (see Fig. 1). $\mathbf{S}_i$, with $|\mathbf{S}_i| = 1$, denotes the localized spin at that site in the insulating layer.

Note that the set-up proposed above is experimentally realizable. In fact, similar interface engineering ideas have been used to study the topological Hall effect in chiral magnetic materials [44–48]. The approximation that exactly one site of the AFM layer is involved in the Hund's coupling is better justified if the interlayer spacing is less than the planar inter-site distance. A similar theoretical proposal to realize AFM skyrmion crystals was recently put forward [49]. However, the proposed model was based on purely classical spins and is hence relevant for insulators. In contrast, the present study retains the role of itinerant electrons, and the mechanism is relevant to SO-coupled metals.

In the case of a strong proximity effect, the coupling between localized spins in the magnetic layer and the electronic spins may be assumed large where double-exchange approximation ($J_H \to \infty$) provides the standard framework for analysis away from the insulating half-filling point. In the large J_H limit, we obtain the Dresselhaus double-exchange (DDE) Hamiltonian [50–52],

$$H_{DDE} = \sum_{\langle ij \rangle, \gamma} [g_{ij}^{\gamma} d_i^{\dagger} d_j + \text{H.c.}] + J_{AF} \sum_{\langle ij \rangle} \mathbf{S}_i \cdot \mathbf{S}_j$$
$$- h_z \sum_i S_i^z, \qquad (2)$$

where, $d_i(d_i^{\dagger})$ annihilates (creates) an electron at site i with spin parallel to the localized spin. The Zeeman coupling of spins to an external magnetic field of strength h_z has been included as the last term in Eq. (2). The projected hopping $g_{ij}^{\gamma} = t_{ij}^{\gamma} + \lambda_{ij}^{\gamma}$ depend on the orientations of the local moments $\mathbf{S}_i$ and $\mathbf{S}_j$ [50,52,53].

III. ANTISKYRMIONS AND AFM ANTISKYRMIONS

We study the DDE Hamiltonian using the hybrid Monte Carlo (HMC) approach that combines the electronic
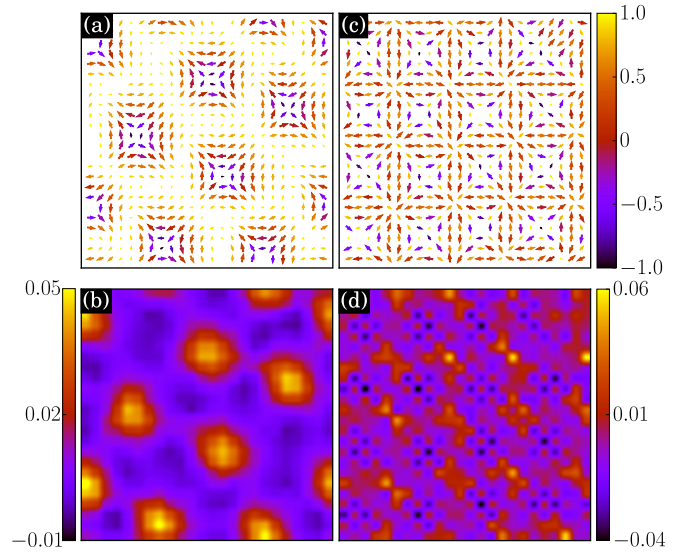
FIG. 2. Snapshots of typical spin configurations [(a),(c)] and the corresponding local skyrmion density [(b),(d)] at $T = 0.001$ for representative values of J_{AF} and h_z as obtained in HMC simulations: [(a),(b)] $J_{AF} = 0.0$, $h_z = 0.03$; [(c),(d)] $J_{AF} = 0.2$, $h_z = 0.45$. The HMC simulations are performed on 24×24 lattice for an average electron filling of 0.3 per site.

diagonalization with the classical Monte Carlo [52,54–56]. All the results discussed below are obtained for $\lambda = 0.4$. We know from the previous detailed studies that the qualitative aspects of results will not change if a more realistic smaller value of SO coupling is used instead [50,53]. The simulations are performed within canonical ensemble approach with the electronic filling fraction kept constant at $n_e = 0.3$. Note that in the double exchange limit, the qualitative properties do not depend on the choice of n_e. Presence of skyrmions or antiskyrmions is inferred from the local skyrmion densities [34,57],

$$\mathcal{T}_i = \frac{1}{8\pi} [\mathbf{S}_i \cdot (\mathbf{S}_{i+x} \times \mathbf{S}_{i+y}) + \mathbf{S}_i \cdot (\mathbf{S}_{i-x} \times \mathbf{S}_{i-y})]. \qquad (3)$$

Representative spin configurations in the magnetic states obtained at low temperature (T) via HMC simulations are shown in Fig. 2. For small J_{AF}, the antiskyrmion state that is present at $J_{AF} = 0$ continues to be stable [50]. The formation of the antiskyrmions is confirmed by the spin configuration [see Fig. 2(a)] as well as the skyrmion density map [see Fig. 2(b)] at low temperatures. The opposite signs of $\mathcal{T}$ and polarity on the central spin characterize the textures as antiskyrmions. We find an exotic AFM antiskyrmion crystal (AF-ASkX) state at $J_{AF} = 0.2$ and $h_z = 0.45$ [see Fig. 2(c)]. The AF-ASkX state can be considered as a superposition of AFM and antiskyrmion configurations. This is reflected in the local skyrmion density map as a checkerboard pattern inside the antiskyrmion cores [see Fig. 2(d)]. Note that there are no explicit spin-spin interaction terms in the Hamiltonian Eq. (2), and above discussed exotic magnetic phases are stabilized by only the long-range interactions mediated via conduction electrons. The AFM antiskyrmion phase obtained within HMC simulations motivates a careful exploration of the phase space. Furthermore, it is also important to understand if an

effective Hamiltonian for spins, obtained by integrating out the electrons, is capable of describing this conversion to AFM antiskyrmions. In the following, we present results on the effective spin-only model that allows access to much larger lattice sizes in comparison to HMC.

IV. AFM ANTISKYRMIONS IN THE EFFECTIVE SPIN MODEL

Derivation of an effective spin model for the Hamiltonian Eq. (2), for the case of Rashba SOC, has already been carried out [8,53]. The effective spin Hamiltonian for the case of Dresselhaus SOC is given by [50,52]

$$H_{\text{eff}} = -\sum_{\langle ij \rangle} D_{ij}^{x(y)} f_{ij}^{x(y)} + J_{\text{AF}} \sum_{\langle ij \rangle} \mathbf{S}_i \cdot \mathbf{S}_j - h_z \sum_i S_i^z,$$

$$f_{ij}^{x(y)} = \frac{1}{\sqrt{2}} \Big[t_{x(y)}^2 \{ 1 + \mathbf{S}_i \cdot \mathbf{S}_j \} - (+) 2t\lambda \hat{x}(\hat{y}) \cdot \{ \mathbf{S}_i \times \mathbf{S}_j \}$$
$$+ \lambda^2 \{ 1 - \mathbf{S}_i \cdot \mathbf{S}_j + 2 \{ \hat{x}(\hat{y}) \cdot \mathbf{S}_i \} \{ \hat{x}(\hat{y}) \cdot \mathbf{S}_j \} \} \Big]^{1/2}. \quad (4)$$

While $D_{ij}^{x(y)}$ can, in principle, be ij and n_e dependent, it has been shown that $D_{ij}^{x(y)} \equiv D_0$ is a very good approximation to study the magnetic phase diagrams of the model Hamiltonian Eq. (2) [53]. For the effective spin model, we use $D_0 = 1$ as the basic energy unit. This change of scale explains the difference in the range of h_z and J_{AF} values required for obtaining similar phases in HMC and effective Hamiltonian calculations. The value of $D_0/|t_\gamma|$ can be obtained for a given value of n_e, and it turns out to be 0.36 for $n_e = 0.3$.

We simulate H_{eff} Eq. (4) using the classical Monte Carlo [58] approach based on the Metropolis algorithm [59,60]. The $J_{\text{AF}} = 0$ limit of the model has been discussed in Ref. [53,56], where a state consisting of filamentary domain wall (fDW) structures was found to be stable at low but finite temperature and at small λ and h_z. Increasing magnetic field leads to packed-skyrmion (pSk) and sparse-skyrmion (sSk) states, and finally to the trivial saturated ferromagnetic (FM) state. Note that fDW to pSk to sSk was obtained for the case of Rashba SOC. For the case of Dresselhaus SOC, the corresponding evolution of phases becomes fDW to pASk to sASk [50]. The effect of AFM exchange coupling between the localized spins is summarized in the form of a low-temperature phase diagram in the h_z-J_{AF} plane (see Fig. 3). The phase boundaries are inferred from the field-dependence of magnetic susceptibility (χ_M), topological susceptibility ($\chi_{\mathcal{T}}$) [61] and spin structure factor SSF [$S_f(\mathbf{q})$] [52]. The phase diagram consists of fDW, packed antiskyrmion (pASk), sparse antiskyrmion (sASk), antiskyrmion square lattice (ASk-SL), and an exotic AFM antiskyrmion crystal (AF-ASkX) along with the relatively trivial single-Q (SQ) spiral, saturated ferromagnetic (FM), and canted antiferromagnetic (CAF) states. In the small J_{AF} limit the fDW state continues to be stable. Increasing J_{AF} leads to a SQ spiral state which remains stable up to very large J_{AF} for low magnetic fields. The instability of fDW can be understood in terms of lifting of degeneracies, by the AFM term, that stabilize the fDW state in the first place [53]. Increasing magnetic field leads to pASk and sASk states for small J_{AF}. In the pASk state, the antiskyrmions are arranged on a triangular lattice [see Fig. 4(a)]. The hexagonal arrangement of anti-
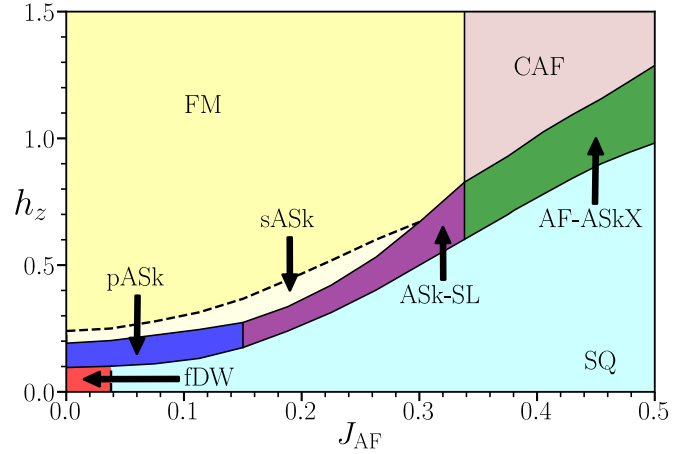
FIG. 3. Low temperature ($T = 0.001D_0$) h_z vs J_{AF} phase diagram. Along with saturated ferromagnetic (FM), canted antiferromagnetic (CAF), and single-Q spiral states, several exotic magnetic phases are confirmed. These are: (i) filamentary domain wall (fDW), (ii) packed-antiskyrmion (pASk), (iii) sparse-antiskyrmion (sASk), (iv) antiskyrmion square lattice (ASk-SL), and (v) AFM antiskyrmion crystal (AF-ASkX). Note that J_{AF} and h_z are in units of D_0, and $D_0/|t_\gamma| \approx 0.36$ for $n_e = 0.3$.

skyrmions becomes more clear in the corresponding SSF plot [see Fig. 5(a)]. The hexagonal peak structure in the SSF can be understood as a superposition of three degenerate spiral states, and the peak at $(0, 0)$ corresponds to the uniform magnetization. We also find that, within the pASk phase, increasing J_{AF} leads to a reduction in the size of antiskyrmions [52]. Generally, one needs to change the strength of SO coupling relative to the bandwidth in order to control the size of these topological magnetic textures. It is a fact of possible practical importance that J_{AF} turns out to be an independent model parameter that can alter the antiskyrmions size. For a range of values, J_{AF} seems to be playing the role of an additive factor to the SO coupling. Following our previous paper, the sASk state can be identified as a metastable state at $T = 0$ [50,56]. Therefore, we mark the sASk-FM boundary with a dotted line. Since, in the sASk state, isolated antiskyrmions exist in the ferromagnetic background [52] the SSF does not show any characteristic pattern for this state.

Over a wide range of J_{AF} values, $0.15 < J_{\text{AF}} < 0.34$, antiskyrmion square lattice (ASk-SL) state is favored in the presence of magnetic field. A similar state is known to exist in the absence of magnetic field for a narrow range of SO coupling values near $\lambda = 1.5$ and at $J_{\text{AF}} = 0$ [53,56]. It is interesting to note that not only the AFM coupling increases the range of stability, it also significantly reduces the values of λ at which the ASk-SL state exists. At large J_{AF}, we find an exotic AFM antiskyrmion crystal (AF-ASkX) state in the range $0.34 < J_{\text{AF}} < 0.5$. This state can be viewed as a superposition of two spin helices, with wave vectors (Q, Q) and $(-Q, Q)$ [see Fig. 5(c)]. The closeness of the peaks to (π, π) reflects the AFM character of the textures. In order to better realize the underlying spin structure of the AF-ASkX, we plot the sublattice resolved spin configuration in Figs. 4(c) and 4(d). The spin textures on individual sublattices in the AF-ASkX state make the tilted square arrangement of antiskyrmions apparent.
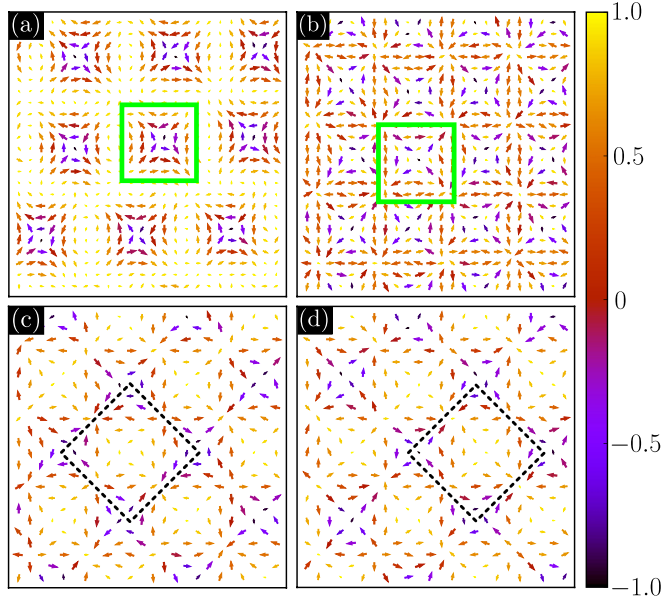
FIG. 4. Snapshots of typical spin configurations at $T = 0.001$ for, (a) pASk at $J_{AF} = 0.03D_0$, $h_z = 0.13D_0$ and (b) AF-ASkX at $J_{AF} = 0.48D_0$, $h_z = 1.1D_0$. The planar components of the spin vectors are represented by the arrows, while the z component is color-coded. We have displayed a 24×24 section of the 40×40 lattice used for simulations. The green boxes enclose a single antiskyrmion or AFM antiskyrmion. The sublattice resolved spin configuration of AF-ASkX state, panel (b), are shown in (c) and (d). The black dotted squares in (c) and (d) indicate the magnetic unit cell of the tilted square lattice.

The skyrmion density ($\mathcal{T}_i$) plots reveal the detailed nature of the AFM-antiskyrmion lattice states. The positive polarity of $\mathcal{T}_i$ in the pASk state is consistent with the result obtained by HMC simulation [compare Figs. 5(b) and 2(b)]. Depending on
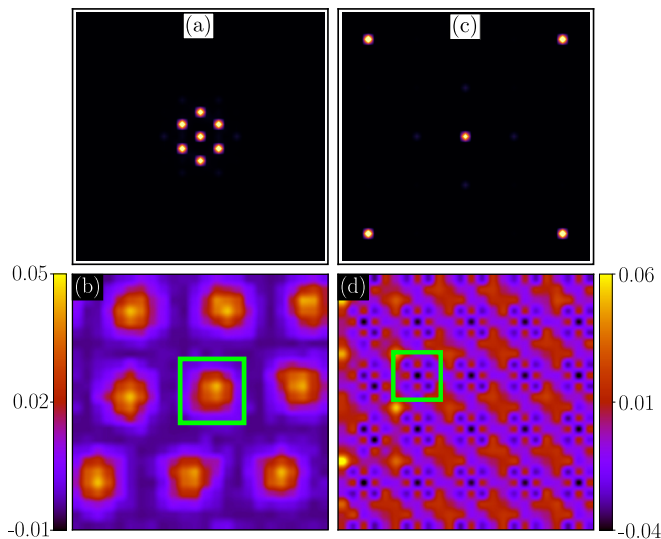
FIG. 5. Locations of peak in the first Brillouin zone in the SSF for the pASk state at (a) $J_{AF} = 0.03$, $h_z = 0.13$ and (c) the AF-ASkX state at $J_{AF} = 0.48$, $h_z = 1.1$. The lower panels (b) and (d) display the corresponding skyrmion density maps.
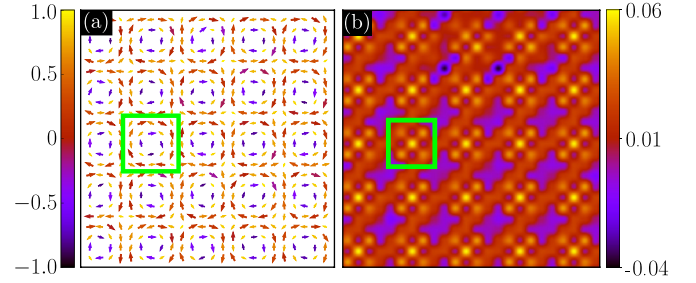
FIG. 6. (a) A typical spin configuration of the AF-BSkX state. The planar spin components are represented by arrows and the information about the z component is color-coded according to the left color bar. (b) Local skyrmion density map for AF-BSkX state at $J_{AF} = 0.48D_0$, $h_z = 1.1D_0$. The results are obtained using HMC simulations of H_{DDE} Eq. (2).

the sublattice, the central spins inside the antiskyrmions are up or down [see Figs. 5(d), 4(c), and 4(d)] [52].

A simple understanding of the three most important phases, pASk, ASk-SL and AF-ASkX, is achieved by inspecting the competition of J_{AF} term with the coupling mediated by electrons. The latter comes in three flavours, as is clear from the three terms under the square root in the definition of f_{ij}^γ [Eq. (4)]: isotropic, DM-like and Kitaev-like terms. Note that the isotropic part is ferromagnetic (antiferromagnetic) for small (large) λ. The J_{AF} term supports the isotropic component of the λ term. For small J_{AF}, the pASk state that is present for $J_{AF} = 0$ continues to exist. In the intermediate J_{AF} region, the anisotropic terms dominate due to a near cancellation of the isotropic part. Note that such a cancellation also exists for $J_{AF} = 0$, if $|t_\gamma| \approx \lambda$. Indeed, a square lattice skyrmion phase was found to be the ground state for $\lambda \approx |t_\gamma|$ [53]. Large J_{AF} favors antiferromagnetism, and the DM-like anisotropic terms lead to the formation of AF-ASkX state.

V. AFM ANTISKYRMION TO AFM BLOCH-SKYRMION

In a recent paper, we have shown that a relative sign change of the electronic hopping parameters leads to conversion of antiskyrmions into Bloch skyrmions [50]. We explicitly show that a change of sign, $t_x \rightarrow -t_x$, in the starting Hamiltonian converts the AF-ASkX discussed above into AFM Bloch skyrmion crystal (AF-BSkX). This is relevant for metals that show band-structure energy extremum away from the Γ point [62–65]. The spin configuration in the ground state of the model H_{DDE} at $J_{AF} = 0.48D_0$ and $h_z = 1.1D_0$ is displayed in Fig. 6. The Bloch character of spin textures is easily visible from the directions of the planar projections of spins. The $\mathcal{T}_i$ maps for the AF-BSkX states [see Fig. 6(b)] display bright spots at skyrmion cores in clear contrast to dark spots seen in the case of AF-ASkX [see Fig. 5(d)]. We provide further understanding of the above conversion to AF-BSkX state with the help of a transformation on spin space of our effective spin model Eq. (4). The anisotropic hopping choice ($t_x \rightarrow -t_x$, $t_y \rightarrow t_y$) leads to a transformation in the spin space, $(S_x, S_y, S_z) \overset{\mathcal{R}_1}{\longmapsto} (S_x, -S_y, S_z)$, such that the energy remains invariant. It can be checked that this transformation in the spin space turns an AF-ASkX to an AF-BSkX state. This finding further establishes the importance of electronic

hopping parameters, and hence the details of the band structure, in determining the intrinsic nature of topological magnetic textures.

Although we have presented all the results for Dresselhaus SO coupling, it is easy to generalize the findings to the case of Rashba SO coupling. For $t_x = t_y$, the Rashba term prefers Néel skyrmions. Therefore, these will be turned into AFM Néel skyrmions in the presence of J_{AF}. For $t_x = -t_y$, the Rashba term will stabilize the antiskyrmions, and therefore J_{AF} will turn these into AFM-antiskyrmions. Since the physics is similar, one can draw conclusions regarding the effect of J_{AF} for the Rashba case even without explicit calculations. In Rashba case, the spin transformation matrix which maps the Néel skyrmions to the antiskyrmions, due to sign-change of relative hopping parameter t_y/t_x, is given by $(S_x, S_y, S_z) \xmapsto{\mathcal{R}_2} (-S_x, S_y, S_z)$. The transformation in the spin space which takes configurations obtained in the Dresselhaus case to those in the Rashba case can be derived from the corresponding $f_{ij}^{x(y)}$ [50,53]. The transformation, which comes out to be $(S_x, S_y, S_z) \xmapsto{\mathcal{R}_3} (-S_y, -S_x, S_z)$, is also evident from the continuum forms of the Rashba and the Dresselhaus SO couplings. Indeed, the transformation $\mathcal{R}_3$ applied to quantum spin maps $H_{DSO} = \lambda_D(\sigma_x k_x - \sigma_y k_y)$ on to $H_{RSO} = \lambda_R(\sigma_x k_y - \sigma_y k_x)$. Therefore, the effective Hamiltonian provides an elegant route to understand the nature of topological textures that are stable for different types of SO couplings and for different relative hopping signs.

VI. CONCLUSION

We have proposed a general approach to tune skyrmions (antiskyrmions) into AFM skyrmions (antiskyrmions) in metallic layers with the help of interface engineering. Recent experiments report the presence of antiskyrmions in inverse Heusler metals lacking intrinsic inversion symmetry [66–68]. We predict that such antiskyrmions can be turned into AFM antiskyrmions at the interface by growing an AFM insulator on top of these inverse Heusler metals. The typical parameter values, from Fig. 3, that are required for realizing the AFM-ASkX or AFM-BSkX phases are $J_{AF} = 0.4D_0$ and $h_z = 0.8D_0$. Since D_0 itself can be tuned via the filling fraction, in addition to the bandwidth, the model provides sufficient flexibility on the choice of parameters that support the interesting AFM skyrmion phases. While the HMC simulations provide numerically accurate results about the nature of magnetic textures, the effective Hamiltonian approach provides a deeper insight into the origin of such topological textures. Furthermore, the form of effective Hamiltonian helps in identifying the mappings in spin space that solve the problem for different types of SO couplings and different choices of relative sign of t_y/t_x without explicit calculations. In particular, these transformations assist us in understanding the conversion of AF-ASkX into AF-BSkX, which is obtained in explicit calculations. We also find that the ASk-SL state, which is known to be stable for rather large values of the SO coupling at $J_{AF} = 0$, is stabilized for lower values of SO coupling at finite J_{AF}. This suggests that J_{AF} is acting as an additive term to the SO coupling for a range of parameters. A direct consequence, which we have explicitly verified, of this hypothesis is that a reduction in the skyrmion size should occur in systems that support an AFM coupling along with a SO coupling. We believe that our paper will motivate further experimental studies for the realization of technologically superior AFM counterparts of skyrmions and antiskyrmions.

[1] A. Fert, N. Reyren, and V. Cros, Nat. Rev. Mater. **2**, 17031 (2017).

[2] Y. Tokura, M. Kawasaki, and N. Nagaosa, Nat. Phys. **13**, 1056 (2017).

[3] T. Jungwirth, X. Marti, P. Wadley, and J. Wunderlich, Nat. Nanotechnol. **11**, 231 (2016).

[4] N. Nagaosa and Y. Tokura, Nat. Nanotechnol. **8**, 899 (2013).

[5] A. N. Bogdanov and C. Panagopoulos, Phys. Today **73**, 44 (2020).

[6] R. Wiesendanger, Nat. Rev. Mater. **1**, 16044 (2016).

[7] A. Fert, V. Cros, and J. Sampaio, Nat. Nanotechnol. **8**, 152 (2013).

[8] S. Banerjee, J. Rowland, O. Erten, and M. Randeria, Phys. Rev. X **4**, 031045 (2014).

[9] W. Pan, J. L. Reno, and A. P. Reyes, Sci. Rep. **10**, 7659 (2020).

[10] C. Wang, H. Du, X. Zhao, C. Jin, M. Tian, Y. Zhang, and R. Che, Nano Lett. **17**, 2921 (2017).

[11] S.-G. Je, H.-S. Han, S. K. Kim, S. A. Montoya, W. Chao, I.-S. Hong, E. E. Fullerton, K.-S. Lee, K.-J. Lee, M.-Y. Im *et al.*, ACS Nano **14**, 3251 (2020).

[12] D. Cortés-Ortuño, W. Wang, M. Beg, R. A. Pepper, M.-A. Bisotti, R. Carey, M. Vousden, T. Kluyver, O. Hovorka, and H. Fangohr, Sci. Rep. **7**, 4060 (2017).

[13] S. Hayami, Phys. Rev. B **103**, 224418 (2021).

[14] X. Yu, N. Kanazawa, W. Zhang, T. Nagai, T. Hara, K. Kimoto, Y. Matsui, Y. Onose, and Y. Tokura, Nat. Commun. **3**, 988 (2012).

[15] Y. Luo, S.-Z. Lin, M. Leroux, N. Wakeham, D. M. Fobes, E. D. Bauer, J. B. Betts, J. D. Thompson, A. Migliori, M. Janoschek *et al.*, Commun. Mater. **1**, 83 (2020).

[16] F. Jonietz, S. Mühlbauer, C. Pfleiderer, A. Neubauer, W. Münzer, A. Bauer, T. Adams, R. Georgii, P. Böni, R. A. Duine *et al.*, Science **330**, 1648 (2010).

[17] R. Yambe and S. Hayami, Sci. Rep. **11**, 11184 (2021).

[18] S. Hayami and Y. Motome, Phys. Rev. B **99**, 094420 (2019).

[19] T. Kurumaji, T. Nakajima, M. Hirschberger, A. Kikkawa, Y. Yamasaki, H. Sagayama, H. Nakao, Y. Taguchi, T.-h. Arima, and Y. Tokura, Science **365**, 914 (2019).

[20] S. Wang, Q. Zeng, D. Liu, H. Zhang, L. Ma, G. Xu, Y. Liang, Z. Zhang, H. Wu, R. Che *et al.*, ACS Appl. Mater. Interfaces **12**, 24125 (2020).

[21] G. Chen, Nat. Phys. **13**, 112 (2017).

[22] D. Toscano, J. Mendonça, A. Miranda, C. de Araujo, F. Sato, P. Coura, and S. Leonel, J. Magn. Magn. Mater. **504**, 166655 (2020).

[23] B. Göbel, A. Mook, J. Henk, and I. Mertig, Phys. Rev. B **99**, 020405(R) (2019).

[24] C. A. Akosa, H. Li, G. Tatara, and O. A. Tretiakov, Phys. Rev. Applied **12**, 054032 (2019).

[25] L. Shen, J. Xia, G. Zhao, X. Zhang, M. Ezawa, O. A. Tretiakov, X. Liu, and Y. Zhou, Phys. Rev. B **98**, 134448 (2018).

[26] K. Litzius, I. Lemesh, B. Krüger, P. Bassirian, L. Caretta, K. Richter, F. Büttner, K. Sato, O. A. Tretiakov, J. Förster *et al.*, Nat. Phys. **13**, 170 (2017).

[27] J. Barker and O. A. Tretiakov, Phys. Rev. Lett. **116**, 147203 (2016).

[28] S. Gao, H. D. Rosales, F. A. G. Albarracín, V. Tsurkan, G. Kaur, T. Fennell, P. Steffens, M. Boehm, P. Čermák, A. Schneidewind *et al.*, Nature (London) **586**, 37 (2020).

[29] T. Dohi, S. DuttaGupta, S. Fukami, and H. Ohno, Nat. Commun. **10**, 5153 (2019).

[30] C. A. Akosa, O. A. Tretiakov, G. Tatara, and A. Manchon, Phys. Rev. Lett. **121**, 097204 (2018).

[31] H. D. Rosales, D. C. Cabra, and P. Pujol, Phys. Rev. B **92**, 214439 (2015).

[32] P. F. Bessarab, D. Yudin, D. R. Gulevich, P. Wadley, M. Titov, and O. A. Tretiakov, Phys. Rev. B **99**, 140411(R) (2019).

[33] X. Liang, J. Xia, X. Zhang, M. Ezawa, O. A. Tretiakov, X. Liu, L. Qiu, G. Zhao, and Y. Zhou, Appl. Phys. Lett. **119**, 062403 (2021).

[34] X. Zhang, Y. Zhou, and M. Ezawa, Sci. Rep. **6**, 24795 (2016).

[35] A. Mukherjee, D. S. Kathyat, and S. Kumar, Phys. Rev. B **103**, 134424 (2021).

[36] A. Mukherjee, D. S. Kathyat, and S. Kumar, Sci. Rep. **11**, 9566 (2021).

[37] S. Seki, X. Yu, S. Ishiwata, and Y. Tokura, Science **336**, 198 (2012).

[38] T. Adams, A. Chacon, M. Wagner, A. Bauer, G. Brandl, B. Pedersen, H. Berger, P. Lemmens, and C. Pfleiderer, Phys. Rev. Lett. **108**, 237204 (2012).

[39] T. Kurumaji, T. Nakajima, V. Ukleev, A. Feoktystov, T.-h. Arima, K. Kakurai, and Y. Tokura, Phys. Rev. Lett. **119**, 237201 (2017).

[40] S. Bordács, A. Butykai, B. G. Szigeti, J. S. White, R. Cubitt, A. O. Leonov, S. Widmann, D. Ehlers, H.-A. K. von Nidda, V. Tsurkan *et al.*, Sci. Rep. **7**, 7584 (2017).

[41] N. D. Khanh, T. Nakajima, X. Yu, S. Gao, K. Shibata, M. Hirschberger, Y. Yamasaki, H. Sagayama, H. Nakao, L. Peng *et al.*, Nat. Nanotechnol. **15**, 444 (2020).

[42] T. Tanigaki, K. Shibata, N. Kanazawa, X. Yu, Y. Onose, H. S. Park, D. Shindo, and Y. Tokura, Nano Lett. **15**, 5438 (2015).

[43] W. Legrand, D. Maccariello, F. Ajejas, S. Collin, A. Vecchiola, K. Bouzehouane, N. Reyren, V. Cros, and A. Fert, Nat. Mater. **19**, 34 (2020).

[44] Q. Shao, Y. Liu, G. Yu, S. K. Kim, X. Che, C. Tang, Q. L. He, Y. Tserkovnyak, J. Shi, and K. L. Wang, Nat. Electron. **2**, 182 (2019).

[45] X. Zhang, Y. Zhou, and M. Ezawa, Nat. Commun. **7**, 10293 (2016).

[46] A. S. Ahmed, A. J. Lee, N. Bagués, B. A. McCullian, A. M. Thabt, A. Perrine, P.-K. Wu, J. R. Rowland, M. Randeria, P. C. Hammel *et al.*, Nano Lett. **19**, 5683 (2019).

[47] Y. Cheng, S. Yu, M. Zhu, J. Hwang, and F. Yang, Phys. Rev. Lett. **123**, 237206 (2019).

[48] P. Zhang, J. Finley, T. Safi, and L. Liu, Phys. Rev. Lett. **123**, 247206 (2019).

[49] B. Göbel, A. Mook, J. Henk, and I. Mertig, Phys. Rev. B **96**, 060406(R) (2017).

[50] D. S. Kathyat, A. Mukherjee, and S. Kumar, Phys. Rev. B **104**, 184434 (2021).

[51] S. Kumar and P. Majumdar, Eur. Phys. J. B **46**, 315 (2005).

[52] See Supplemental Material at http://link.aps.org/supplemental/10.1103/PhysRevB.105.075102 for the derivation of the effective spin model, the details of the simulation methods and the characterization of different phases.

[53] D. S. Kathyat, A. Mukherjee, and S. Kumar, Phys. Rev. B **102**, 075106 (2020).

[54] S. Kumar and P. Majumdar, Eur. Phys. J. B **50**, 571 (2006).

[55] A. Mukherjee, N. D. Patel, C. Bishop, and E. Dagotto, Phys. Rev. E **91**, 063303 (2015).

[56] D. S. Kathyat, A. Mukherjee, and S. Kumar, Phys. Rev. B **103**, 035111 (2021).

[57] J. Chen, D.-W. Zhang, and J.-M. Liu, Sci. Rep. **6**, 29126 (2016).

[58] K. Binder, D. Heermann, L. Roelofs, A. J. Mallinckrodt, and S. McKay, Comput. Phys. **7**, 156 (1993).

[59] N. Metropolis, A. W. Rosenbluth, M. N. Rosenbluth, A. H. Teller, and E. Teller, J. Chem. Phys. **21**, 1087 (1953).

[60] W. K. Hastings, Biometrika **57**, 97 (1970).

[61] D. Amoroso, P. Barone, and S. Picozzi, Nat. Commun. **11**, 5784 (2020).

[62] K. V. Shanavas and S. Satpathy, Phys. Rev. B **93**, 195101 (2016).

[63] H. Choi, Y.-Y. Tai, and J.-X. Zhu, Phys. Rev. B **99**, 134437 (2019).

[64] T. Nomoto, T. Koretsune, and R. Arita, Phys. Rev. Lett. **125**, 117204 (2020).

[65] T. Koretsune, N. Nagaosa, and R. Arita, Sci. Rep. **5**, 13302 (2015).

[66] A. K. Nayak, V. Kumar, T. Ma, P. Werner, E. Pippel, R. Sahoo, F. Damay, U. K. Rößler, C. Felser, and S. S. Parkin, Nature (London) **548**, 561 (2017).

[67] P. Vir, N. Kumar, H. Borrmann, B. Jamijansuren, G. Kreiner, C. Shekhar, and C. Felser, Chem. Mater. **31**, 5876 (2019).

[68] J. Jena, R. Stinshoff, R. Saha, A. K. Srivastava, T. Ma, H. Deniz, P. Werner, C. Felser, and S. S. P. Parkin, Nano Lett. **20**, 59 (2020).